Research Square

Preprints are preliminary reports that have not undergone peer review.
They should not be considered conclusive, used to inform clinical practice,
or referenced by the media as validated information.

CVD Multilayer Boron Nitride-encapsulated graphene Solution-Gated Field-Effect Transistors for wearable and implantable biosensors

Carole-Anne Lernoud
Université Grenoble Alpes
Lionel Rousseau
University Gustave Eiffel
Vincent Bouchiat
Grapheal SAS
Blaise Yvert
Université Grenoble Alpes
Clément Hébert
clement.hebert@inserm.fr

Université Grenoble Alpes

Article

Keywords:

Posted Date: October 30th, 2026

DOI: https://doi.org/10.21203/rs.3.rs-11233364/v1

License: This work is licensed under a Creative Commons Attribution 4.0 International License.
Read Full License

Additional Declarations: No competing interests reported.

Abstract

Great efforts are currently devoted to the development of graphene Solution-Gated Field-effect transistors (gSGFET) as sensors for biosensing applications and particularly, neural implants. Indeed, with the high carrier mobility of graphene, graphene-based sensors exhibit very high sensitivity and the easy integration of graphene in flexible devices is a clear advantage for implantable technologies by reducing rejection from biological tissues. However, despite the great performances already exhibited by gSGFETs for biosensing, this technology has not shown its full potential yet. This is due to the fact that since the graphene channel is in direct contact with the liquid medium, the carrier mobility, and consequently the sensitivity of a gSGFET, stays below its theoretical value and the sensors performances are subjected to stability issues. Hexagonal Boron Nitride (hBN) has been proved to be a key two-dimensional material that will enable to overcome carrier mobility limitations. Because the access to highly pure large scale-hBN is challenging, we tested here whether more accessible lower-quality commercial Chemical Vapor Deposited Multilayer BN could still be successfully used to improve gSGFETs sensitivity for neural recordings. We demonstrate that even when using a commercial multilayer BN, the performances of gSGFET sensors can be improved to enable neural recording.

1. Introduction

Wearable and implantable biosensors hold great promise for accurate diagnosis and healthcare monitoring such as glucose sensing, oxygen monitoring, electrocardiograms or neural recording[1–5]. One key feature to achieve the ideal devices for the patient and the daily use of these biosensors is the flexibility and the conformability of the sensors. Consequently, prevailing sensor technologies for healthcare rely on flexible polymer substrates and flexible transducers[6,7]. Among the massive panel of flexible materials for transducer, graphene appears as one of the few that combines high electronic performances, fabrication reproducibility and straightforward integration on microelectronic processes[8]. Moreover, single-layer graphene (SLG) has been shown to be biocompatible[9] and its atomic flatness allows for the integration into ultra-thin or bioresorbable flexible substrates, thus offering the possibility to design implantable biosensors with a minimal footprint in the body. Consequently, gSGFET were reported for glucose sensor[10], DNA sensing[11], SARS-COV2 detection[12], electrocardiograms[13], wide bandwidth neural recording[14] and many others. Nevertheless, the performance of gSGFETs when used as biosensors are still far from the full potential of the SLG material. Indeed, most of the studies highlight that graphene mobility in biosensor is rather low compare to its theoretical values and that impurities in the graphene environment induce charge traps and mobility fluctuations[15–17]. These two parameters strongly alter the sensing capability of the gSGFETs by affecting both the transconductance (sensitivity) and the noise limit. To overcome these limitations, several studies have suggested to encapsulate single layer graphene to preserve its outstanding electronic properties. Encapsulation or passivation with Ta_2O_5[18], CaF_2[18] or Hexagonal Boron Nitride (hBN) [19–21] were thus suggested to increase the graphene mobility and to reduce the channel noise. Among these strategies, hBN has been proved to be one of the key materials to preserve the graphene high mobility even at room temperature

but also to reduce mobility fluctuation and consequently the noise limit of the gSGFET[22,23]. In addition, the use of hBN was proved to extend the lifetime of the gSGFET by protecting the graphene layer from the oxidation at the liquid interface[24,25]. Most of the studies reported so far were performed using highly pure hBN crystal obtained by exfoliation. However, the production of high-quality hBN on large surface is still being developed and is not accessible on the market. In the present study, we evaluate the impact of the encapsulation of Chemical Vapor Deposited (CVD) graphene with already available commercial multilayer 2D-BN on the sensitivity and on noise of graphene gSGFET. To do so, we fabricated on the same 4" silicon wafer bare gSGFET and BN-encapsulated gSGFET to compare the sensitivity and noise of the devices. The study was performed on 96 BN-encapsulated gSGFETs and 96 bare gSGFETs dispatched over different regions of the wafer to ensure a statistical relevance of the results. By fabricating transistors with variable length, we use the Transfer Length Method (TLM) approximation to extract the R_{sheet}, R_c and mobility (μ) of the transistor in order to decipher the impact of the BN encapsulation. We first considered rigid substrates and then fabricated flexible gSGFETs on polyimide in order evaluate the possibility to measure electrogenic cell activity. We proved that BN encapsulation, even with low-quality CVD BN can already improve the transconductance and the intrinsic noise of gSGFETs for wearable and implantable applications.

2. Material and methods

2D Materials

Multilayer BN on copper foil was purchased from 2D SEMICONDUTOR (Ref CVD-hBN-CU-MU). Single layer graphene was provided by GRAPHEAL SAS on copper foil.

Wet transfer process: The BN and Graphene layers were received on copper foils. A layer of Poly(Methyl Methacrylate) (PMMA, KAYAKU) A4 is spined at 3000 rpm on the Copper foil on the face covered with the 2D material and dried in air for 30 min. The copper foil is placed on a 4 inch silicon wafer using Kapton tape with the PMMA facing the wafer and exposed to a soft plasma to remove any backside material (O_2 for graphene and CH_4 for BN, 4W RF, 200W ICP, 50sccm, 2min). The copper foil exposed to the plasma is gently cut with a blade and placed in a bath of $FeCl_3$:HCl over night to etch the copper. The 2D material/PMMA is then fished using a clean silicon dioxide wafer in two successive baths of deionised water for a duration 3h each to remove any residue of copper. The cleaned 2D material/PMMA layer is fished on position on the final wafer. The wafer is placed on a hot plate at 45°C for 1h and slowly ramped (5°C/min) to 90°C and maintained at 90°C for 1h. The wafer is immersed in acetone for 30 min and flushed with isopropanol to remove the PMMA.

Test Device on SiO_2 fabrication

The test devices on SiO_2 consists of 4 lines of 14 transistors and 2 source contacts presented in Fig. 1b. Twelve gSGFETs have a length of 40μm and are distributed by pair of L = 5μm, 10μm, 20μm, 40μm and 60μm. Two gSGFETs are either 100μmx100μm, 60μmx60μm, 10μmx10μm or 5μmx5μm. The devices

were fabricated in cleanroom environment following the schematics presented in Fig. 1a. First, a Ti/Au metal deposition by UV photolithography followed by e-beam evaporation ($1nm.s^{-1}$ and $10nm.s^{-1}$) were performed to delineate the regions where BN must be transferred. Then BN layer (2x2 multilayer BN on copper foil purchased from 2D Semiconductors, Ref CVD-hBN-CU-MU) were transferred using the wet transfer process. Ti/Au metallic contacts were then defined and deposited using UV photolithography with AZ5214E (MicroChemicals GmBH) in negative tone and metal evaporation of Ti and Au at a rate of respectively $1nm.s^{-1}$ and $10nm.s^{-1}$. The graphene layer (provided by Grapheal SAS) was then transferred using the wet transfer process. The graphene channels were defined using positive resin AZ1512HS (MicroChemicals GmBH) as a mask and smoothly etched in an ICP Oxford (O_2 50sccm, RF Power 5W, Coil Power 250W). The mask is removed by acetone and IPA cleaning for 30 min and 10 min. A second metal contact is deposited using the same protocol. A second BN wet transfer is made to cover the full surface of the device. Finally, a SU8 (KAYAKU) layer of 2.5µm is deposited to insulate the tracks and define the channel areas that will be in contact with the liquid. The final device is presented in Fig. 1b.

Flexible device fabrication: The flexible devices consisted of 4x4 arrays of gSGFETs integrated on implants intended for epicortical activity recordings as presented in Fig. 1c. Three different gSGFET geometries were used: 50µmx60µm 40x50µm and 30x40µm. The flexible devices were fabricated with a protocol similar to that of the rigid device. First, a 7-µm-thick 2611HD polyimide film was deposited by spin coating on a 4” Si wafer terminated by a 512nm thermal SiO_2. The film was annealed in a thermal oven at 350°C during 4h under a Nitrogen atmosphere A first BN layer is transferred at the centre of the wafer where ½ of the implants will be positioned using the wet transfer process. Ti/Au metallic contacts were then defined and deposited using UV photolithography with AZ5214E in negative tone and metal evaporation of Ti and Au at a rate of respectively $1nm.s^{-1}$ and $10nm.s^{-1}$. The graphene layer (provided by Grapheal SAS) was then transferred using the wet transfer process. The graphene channels were defined using positive resin AZ1512HS as a mask and smoothly etched in an ICP Oxford (O_2 50sccm, RF Power 5W, Coil Power 250W). The mask is removed by acetone and IPA cleaning for 30 min and 10 min. A second metal contact is deposited using the same protocol. A second BN wet transfer is made to cover the full surface of the device. A SU8 layer of 2.5µm is deposited to insulate the tracks and defines the channel areas that will be in contact with the liquid. The SU8 is only deposited on the implant and not on the full wafer in order to ease the etching of PI to liberate the implants. The implant shape is defined using a AZ40XT (MicroChemicals GmBH) 30µm thick resin. The PI is etched using ICP plasma (O_2/ CH_4, 40sccm/10sccm, RF Power 250W, Coil Power, 500W, 12min). The implants are liberated by pealing them from the wafer with a tweezer. The pealing is easier when a bit of distilled water is dropped on the wafer. The final device is presented in Fig. 1d.

Rigid Transistor Characterizations: The 14 transistors were measured following the electric schematic provided in Figure S1. The 14 drains and the 2 sources were contacted in parallel using a 16 channels DC probe from Form Factor (DC quadrant Probe). A custom electronic card to convert the channel current to voltage and amplified the signal has been fabricated by ID3 Technologies and developed based on a

previous report[26] (details of the card can be given upon request). The card splits the signals between DC (< 0.1Hz) and AC (> 0.1Hz) and is connected to a NI USB6363 to peform the digitization. The same instrument is used to generate V_{gs} and V_{ds}. V_{gs} is applied in the solution using an Ag/AgCl electrode. The set up acquisition protocol is controlled using an updated version of the PyGFET interface available on github (https://github.com/aguimera/PyGFET). The AC and DC source drain currents can be read from the 14 channels in parallel to obtain the transfer curve. The DC current is used to extract the transconductance and predict the sensitivity of the transistor to electric potential variation in the close environment of the graphene, the AC current is used to extract $I_{ds,rms}$ and consequently the equivalent gate noise in order to predict the lowest signals voltage that can be detected by the sensors. All the characterizations were performed in Phosphate Buffered Saline (PBS) 1X. V_{ds} was set at 50mV.

Flexible Transistor Characterizations

The flexible transistors were characterized using the same protocols and set up as for the test devices on SiO_2. An adaptor was designed to connect the 16 drains and 2 sources (Figure S2). The characterizations were performed in PBS (1X). V_{ds} was set at 50mV.

Recording of simulated neuronal signals

A custom system allowing to perform transistor recording with an INTAN RHS system (INTAN technology) was developed in collaboration with Grapheal SAS (Figure S2). It consists in 16 channels for current to voltage conversion and amplified the signal. As for the card used for the DC characterization, the channels are spitted between DC and AC signals. The DC signals are amplified with a gain of 10^5 and the AC signals are amplified with a 10^4 gain. The results presented in this study were only measured on the AC channels. The synthetic signals were applied using a Signal Generator ME/W-SG (Multichannel Systems) on the Ag/AgCl gate electrode. The recordings were performed in PBS 1X. V_{ds} was set to 50mV and V_{gs} was set close to the value at which G_m was found to be the highest.

CNP and Carrier density estimation

The Charge Neutrality Point (CNP) was estimated for each device as the gate voltage at which $|I_{ds}|$ is minimum. For a given material stack (e.g. monolayer graphene or BN–Gr–BN heterostructure), the median of the device-level CNP values was used to define the gate overdrive $V_{GSO} = V_{gs} - CNP$. The gate capacitance per unit area C_g was taken as 2 $\mu F.cm^{-2}$ for monolayer graphene (average value of the double layer capacitance in water; the same value was used by default for the encapsulated devices. The carrier density induced by the gate was calculated as $n = C_g V_{GSO} / e$ where e is the elementary charge ($1.6x10^{-19}C$).

TLM and DTM analysis: Transfer Length Method: Channel sheet resistance R_{sh} and specific contact resistivity ρ_c were extracted using the Transfer-length method following Murros et al[27]. At each gate bias,

the total device resistance was defined as $R_{tot} = |V_{ds}|/|I_{ds}|$. Data points with $R_{tot} > 10^5$ Ω or $|I_{ds}| < 1$ nA were rejected. For a fixed V_{gs}, R_{tot} was plotted as a function of channel length and fitted to the linear relation (figure S3).

$$R_{tot}.W = R_{sh}\, L + 2\, \rho_c, \quad (1)$$

where W and L are the channel width and length, R_{sh} is the sheet resistance ($\Omega\ \square^{-1}$), and ρ_c is the specific contact resistivity (Ω µm). The slope of the linear fit yields Rsh directly; the intercept gives $2\rho_c$. At least three devices and two distinct channel lengths were required for a fit at a given bias. When the fitted slope was non-physical ($R_{sh} \leq 0$, as can occur near the Dirac point), R_{sheet} was re-estimated from the contact-corrected channel resistance ($R_{tot}.W - 2\rho_c$)/L evaluated device by device, and the median was retained.

Field-effect mobility was derived from the Drude relation associated with TLM framework:

$$|\mu| = |1 / (R_{sh}\, C_g\, V_{GSO})| \quad (2)$$

Where C_g Mobility values with $|V_{GSO}| < 0.05$ V were excluded because the carrier density approaches zero near the charge-neutrality point. Sheet resistance and contact resistivity were reported as functions of V_{gs} (or, equivalently, of carrier density n). For comparative statistics, hole mobility |µh| from the gated TLM was read at a reference density $n = 1.10^{-12}$ cm^{-2} by interpolation along the $\mu(V_{GSO})$ curve.

Direct transconductance method (DTM) : Mobility was also determined using the direct transconductance method (DTM), following Murros et al. The transconductance $Gm = \partial I_{ds} / \partial V_{gs}$ was calculated by numerical differentiation of each transfer curve; G_m was evaluated at the midpoints of the V_{gs} sampling grid. The field-effect mobility was then obtained as

$$\mu = G_m / (C_g\, (W/L)\, V_{ds}) \quad (3)$$

where W/L is the channel aspect ratio and V_{ds} is the applied drain voltage. This procedure was applied independently to each transistor. For a given structure, the median mobility at each V_{GSO} was computed after aligning all device curves on a common gate-overdrive axis. As for the gated TLM, points with $|V_{GSO}| < 0.05$ V were excluded. For population comparisons, |µ| was extracted at $n = \pm 1 \times 10^{12}$ cm^{-2} for holes and electrons, respectively.

Statistical Analysis: Group comparisons on boxplots were assessed with non-parametric tests, as device-to-device variability was not assumed to be normally distributed. Each transistor contributed one scalar value (independent samples). Tests were implemented in SciPy. When two structures were compared (e.g. Gr versus BN-Gr-BN), a two-sided Mann–Whitney U test was used. When three or more groups were compared, a Kruskal–Wallis test was applied. A p-value was reported only if each group contained at least two finite values. Significance was annotated as: * $p < 0.05$, ** $p < 0.01$, *** $p < 0.001$,

ns = not significant. Brackets and p-values were drawn above compared boxplots; the test name and legend appeared in the figure footer. Sample size n (number of transistors) was shown beneath each box. Outlier exclusion was applied, values outside the Tukey fences (Q1 − 1.5×IQR, Q3 + 1.5×IQR) were removed before plotting and testing.

3. Results and discussion

The transistor transfer curve (I_{ds} vs V_{gs}) for bare and encapsulated gSGFET on SiO_2 are presented in Fig. 2. The values observed for the drain source current and transconductance of the bare devices are below the state of the art for optimised gSGFET[28] but they are descent compared to the literature[29] showing that the fabrication quality of the bare device can be used as comparison to evaluate the impact of the BN encapsulation. The encapsulation of graphene with BN is supposed to reduce the intrinsic doping of the graphene induced by the interaction with the substrate. The doping level can be estimated by the position of the charge neutrality point (CNP). It can be observed that the CNP is around 0.4V for both configurations and is slightly shifted (9mV) in the case of encapsulated graphene. The inherent doping due to the substrate is thus not dramatically decreased by the intercalation of the BN between the graphene and the SiO_2. Nevertheless, the drain-source current (Fig. 2a) and transconductance (Fig. 2b) are increased when using encapsulated graphene, with mean conductance values across devices increasing from 1.2mS/V to 1.8mS/V (Fig. 2b). The increase of the G_m can be observed for all L values and region on the wafer used for the analysis, and is all the more important that the length of the gate is small, a promising asset for high-density biosensing devices (Fig. 2c).

We also evaluated the evolution of the intrinsic noise with the BN encapsulation. To do so the current power spectral density $S_{I(f)}$ of the I_{ds} current was measured. We first calculated the root mean square of I_{ds} ($I_{ds,rms} = \sqrt{(\int S_{I(f)}\, df)}$). Figure 3a shows the $I_{ds,rms}$ vs V_{gs} curve in the 1 to 100Hz frequency band. One can observe that the current noise level $I_{ds,rms}$ is smaller for the encapsulated channel. The equivalent gate noise which determines the minimum voltage signal that can be measured by the transistor can then be found by dividing the $I_{ds,rms}$ signal by the transconductance for each V_{gs}. Figure 3b shows that the equivalent gate voltage noise is decreased for encapsulated devices whatever the channel length (Fig. 3b). For instance, the mean value for square devices decreases from 200 μV_{rms} to 150 μV_{rms}.

Our main hypothesis is that the sensitivity and the noise of the encapsulated device is improved thanks to a higher mobility in the graphene channel induced by a reduced number of charge traps and coulombic interaction with charge fluctuation in the liquid medium[30]. Nevertheless, the quality of the contact also strongly influences the sensitivity and the intrinsic noise of the gSGFET[28,31]. A low contact resistance results in both high transconductance and low equivalent gate noise. In order to discriminate between the different contributions, we performed a TLM study. From the DC measurement and TLM configuration we could extract the channel resistance R_{Sheet} as well as the contact resistance ρ_c and the mobility μ. We also used the DTM method to extract the mobility.

As shown in Fig. 4a, the TLM analysis shows that our contact resistance is quite large compared to the literature[27,28](best values around 270 Ω.µm[27]) with values around 22kΩ.µm for bare gSGFET. The contact resistance is improved by using the encapsulation structure and is reduced to 17.5k Ω.µm. This reduction of the contact resistance can explain the increase of Gm as described in Schaefer et al[28]. In the meantime, one can also notice from Fig. 4b that R_{sheet} is also decreased for encapsulated structures proving that not only the contact quality is improved but also the channel has a better conductivity when the graphene layer is encapsulated with BN. This improvement of the channel conductivity of gSGFET thanks to the use of multilayer hBN was reported by Petach et al[30]. It is attributed to the reduction of the Coulomb scattering from the PBS that reduces the mobility fluctuations.

For the mobility analysis, we assumed a double-layer capacitance C_{dl} (or C_g) of 2µF.cm^{-2} for both bare and encapsulated graphene which is a high overestimation for encapsulated material because the BN layer decreases the capacitance. Using the TLM approach, we obtained mean mobilities around 2200 cm^2.V^{-1}.s^{-1}. for encapsulated device and 2100 cm^2.V^{-1}.s^{-1} for bare device while these values are only 523 cm^2.V^{-1}.s^{-1} and 367 cm^2.V^{-1}.s^{-1} in the DTM approach (Fig. 4c). The main reason for the discrepancy between the two approaches being that the contact resistance is not considered in the DTM model. The mobility values on SiO_2 are consistent with the literature[27,32]. So, even with an overestimated value of the $C_{dl,}$ an increase of the mobility can be observed whatever the way the mobility was calculated. We can thus infer that the decrease of the channel resistance originates from an increase of the channel mobility.

In order to evaluate the possibility to use encapsulated device for biosensing an especially to record of neural activity, encapsulated gSGFETs were fabricated on polyimide substrate. Figure 5 presents the transistor characterization in PBS. For this configuration, the yield of bare gSGFET was 40% whereas that of the encapsulated devices was 75%, suggesting that the encapsulation allows to preserve the transistor integrity even in case of an alteration in the fabrication process.

Similar to the results obtained on the silicon wafer, the CNP is around 400mV and is slightly decreased (21mV) for the encapsulated devices (Fig. 5a), showing that the BN layer intercalated between the graphene and the PI has only a limited impact on the doping level due to the substrate. The transconductance for encapsulated device is once again larger compared to the bare device with a mean normalized value on all the transistors around 1mS/V per square versus 0.5mS/V per square (Fig. 5b). Compared to the test device on $SiO_{2,}$ the values are decreased by a factor 1.7. Also, the equivalent gate noise decreased from 250 µV rms down to 130 µV rms per square (Fig. 5c). As a consequence of the transconductance decrease, the mobility values extracted from DTM are also lower than the values obtained with the rigid substrates ranging now from 210 cm^2.V^{-1}.s^{-1} for bare device to 402 cm^2.V^{-1}.s^{-1} for the encapsulated ones. (Fig. 5d).

Finally, we performed an *in vitro* evaluation of the capability of encapsulated transistor to record neuronal activity. To do so, a synthetic signal mimicking hippocampal action potentials was applied on the

Ag/AgCl electrode with respect to which the transistors of an array were polarized (Figure S2). The signal contained 3 main spikes exhibiting amplitudes of 300 µV and 150 µV. The measured signal was compared to the synthetic signal by applying the transconductance factor measured in a DC configuration to the raw signal. As shown on Fig. 6a the signal was successfully recorded for 6 gSGFETs of the array among the 15 gSGFETs that were functional according to the DC characterization (Figure S4). Each occurrence of the signal is highlighted by an arrow. It can be seen that all the channels were able to detect the signal. However, only the channel with the highest transconductance (B-023) was able to catch all of them. The mean of the events for the 6 channels is presented in Fig. 6b. The amplitude of the synthetic 300-µV spike measured by the transistors is around 250 µV and 300 µV showing the ability of the encapsulated-gSGFET to properly measure the amplitude of the synthetic signal. The single 300-µV spikes clearly appear above the background noise for all the transistors and for channel B-023, single 150-µV spikes could also be detected. This shows that events as low as 150µV can be detected (Figure S5).

4. Conclusion

In this study, we first performed a study on 176 transistors on rigid SiO_2 substrate to evaluate the impact of the encapsulation of graphene channel with commercial multilayer BN. We show that the encapsulation improved both the transconductance and the intrinsic noise of the transistor. A TLM and mobility analysis shows that the improvement of the performances can be attributed to both a decrease of the contact resistance at the drain and source terminal and an increase of the channel mobility and a reduction of the mobility fluctuations thanks to the screening of the Coulomb scattering. The improvements of the performances of the transistor are also observed on polyimide flexible substrates. We also proved that the flexible transistor performances are less sensitive to alterations in the fabrication process. Indeed, in the very same wafer 75% of the encapsulated transistors where functional while only 45% of the graphene one could still be used. We then showed that encapsulated devices can successfully record neuronal signals with amplitudes as low as 150 µV. In order to further improve the recording quality of these devices, further studies could address the improvement of the contact quality by using for example ozone treatment. Although low-quality BN was used for the study, it allowed to already exhibit high transconductance and noise performance. Working with hBN of controlled and high purity should also dramatically improve the sensitivity of the device. Additionally, the BN layer is supposed to be less sensitive to aging. It would thus be very interesting to test the increase of longevity of gSGFET over time thanks to the BN protective layer. Finally, by reducing the gate capacitance and by further increasing the leakage resistance between the graphene and the liquid medium, this type of device is supposed to be able to work at high frequencies, which would be interesting for wireless and wearable applications where MHz and GHz signals are often used.

Declarations

Author Contribution

CA.L fabricated all the test devices and contributed to the fabrication of the in vivo device. She performed all the characterizations and the data analysis of the test devices and flexible implants and review the manuscript. LR contributed to the design of the devices and to the fabrication of the flexible implants. V.B grew the graphene on copper and contributed to the design of the electronic for the neural recordings with the INTAN card. B.Y participated to the analysis of the data and manuscript reviewing. C.H secured the funding, fabricate the flexible implants, performed the analysis of the recordings for synthetic signals and wrote the main manuscript text.

Acknowledgements and Fundings:

This work was partially supported by the French RENATECH network, implemented at the Upstream Technological Platform in Grenoble (PTA)

This work has been funded by the INSERM/ CNRS ATIP program and the Region Auvergne-Rhône-Alpes through the Pack Ambition Recherche program.

Data Availability

All the data and codes for the data analysis can be accessed upon request by writing to the following address: clement.hebert@inserm.fr

References

1. Lee, S. P. et al. Highly flexible, wearable, and disposable cardiac biosensors for remote and ambulatory monitoring. *npj Digit. Med.* **1**, 1–8 (2018).
2. MacEira-Elvira, P., Popa, T., Schmid, A. C. & Hummel, F. C. Wearable technology in stroke rehabilitation: Towards improved diagnosis and treatment of upper-limb motor impairment. *J. Neuroeng. Rehabil*. **16**, 1–18 (2019).
3. Kwon, S., Kim, H. & Yeo, W. H. Recent advances in wearable sensors and portable electronics for sleep monitoring. *iScience* **24**, 102461 (2021).
4. Pérez, D. & Orozco, J. Wearable electrochemical biosensors to measure biomarkers with complex blood-to-sweat partition such as proteins and hormones. *Microchim Acta 2022*. **1893** (189), 1–28 (2022).
5. Kim, J., Campbell, A. S., de Ávila, B. E. F. & Wang, J. Wearable biosensors for healthcare monitoring. *Nat. Biotechnol.* **37**, 389–406 (2019).
6. Iqbal, S. M. A., Mahgoub, I., Du, E. & Leavitt, M. A. & Asghar, W. Advances in healthcare wearable devices. *npj Flex. Electron.* 5, 1–14 (2021). (2021).
7. Cao, X. et al. Engineering two-dimensional layered nanomaterials for wearable biomedical sensors and power devices. *Mater. Chem. Front.* **2**, 1944–1986 (2018).

8. Hassan Chowdhury, M. K. et al. Sensing the future with graphene-based wearable sensors: A review. *Results Mater.* **25**, 100646 (2025).
9. Bullock, C. J. & Bussy, C. Biocompatibility Considerations in the Design of Graphene Biomedical Materials. *Adv. Mater. Interfaces*. **6**, 1900229 (2019).
10. Lopes, V. et al. Graphene-Based GlucoseSensors with an Attomolar Limitof Detection. *J. Am. Chem. Soc.* **147**, 13059–13070 (2025).
11. Fu, W. et al. Sensing at the Surface of Graphene Field-Effect Transistors. *Adv. Mater.* **29**, 1603610 (2017).
12. Wu, G. et al. Implantable Aptamer-Graphene Microtransistors for Real-Time Monitoring of Neurochemical Release in Vivo. *Nano Lett.* 3677 (2022). (2022).
13. Hlukhova, H., Kireev, D., Offenhäusser, A., Pustovyi, D. & Vitusevich, S. Graphene Field-Effect Transistors toward Study of Cardiac Ischemia at Early Stage. *Adv. Electron. Mater.* **11**, 2400332 (2025).
14. Masvidal-Codina, E. et al. High-resolution mapping of infraslow cortical brain activity enabled by graphene microtransistors. *Nat. Mater.* **18**, 280–288 (2019).
15. Lu, J. et al. Negative correlation between charge carrier density and mobility fluctuations in graphene. *Phys Rev. B - Condens. Matter Mater. Phys* **90**, (2014).
16. Zhang, Y., Mendez, E. E. & Du, X. Mobility-dependent low-frequency noise in graphene field-effect transistors. *ACS Nano*. **5**, 8124–8130 (2011).
17. Balandin, A. A. Low-frequency 1/f noise in graphene devices. *Nat. Nanotechnol*. **8**, 549–555 (2013).
18. Illarionov, Y. Y. et al. Variability and high temperature reliability of graphene field-effect transistors with thin epitaxial CaF2 insulators. *npj 2D Mater. Appl.* 8, 23- (2024). (2024).
19. De Fazio, D. et al. High-Mobility, Wet-Transferred Graphene Grown by Chemical Vapor Deposition. (2019). https://doi.org/10.1021/acsnano.9b02621 doi:10.1021/acsnano.9b02621.
20. Banszerus, L. et al. Ultrahigh-mobility graphene devices from chemical vapor deposition on reusable copper. *Sci. Adv.* **1**, e1500222 (2015).
21. Stolyarov, M. A., Liu, G., Rumyantsev, S. L., Shur, M. & Balandin, A. A. Suppression of 1/ f noise in near-ballistic h -BN-graphene- h- BN heterostructure field-effect transistors. *Appl Phys. Lett* **107**, (2015).
22. Viti, L., Purdie, D. G., Lombardo, A., Ferrari, A. C. & Vitiello, M. S. HBN-Encapsulated, Graphene-based, Room-temperature Terahertz Receivers, with High Speed and Low Noise. *Nano Lett.* **20**, 3169–3177 (2020).
23. Kumar, C., Kuiri, M., Jung, J., Das, T. & Das, A. Tunability of 1/f Noise at Multiple Dirac Cones in hBN Encapsulated Graphene Devices. (2016). https://doi.org/10.1021/acs.nanolett.5b04116 doi:10.1021/acs.nanolett.5b04116.
24. Shautsova, V., Gilbertson, A. M., Black, N. C. G., Maier, S. A. & Cohen, L. F. Hexagonal Boron Nitride assisted transfer and encapsulation of large area CVD graphene. *Sci. Reports* 6, 30210- (2016).

(2016).
25. Mahvash, F. et al. Corrosion resistance of monolayer hexagonal boron nitride on copper. *Sci. Rep.* **2017 71 7**, 42139 (2017).
26. Hébert, C. et al. Flexible Graphene Solution-Gated Field-Effect Transistors: Efficient Transducers for Micro-Electrocorticography. *Adv. Funct. Mater.* https://doi.org/10.1002/adfm.201703976 (2017).
27. Murros, A. et al. Graphene FET Process and Analysis Optimization in 200 mm Pilot Line Environment.
28. Schaefer, N. et al. Improved metal-graphene contacts for low-noise, high-density microtransistor arrays for neural sensing. *Carbon N Y* **161**, (2020).
29. Kireev, D. et al. Graphene transistors for interfacing with cells: towards a deeper understanding of liquid gating and sensitivity. *Sci. Rep.* **2017 71** (7), 6658 (2017).
30. Petach, T. A. et al. Disorder from the Bulk Ionic Liquid in Electric Double Layer Transistors. (2017). https://doi.org/10.1021/acsnano.7b03864 doi:10.1021/acsnano.7b03864.
31. Karnatak, P. et al. Current crowding mediated large contact noise in graphene field-effect transistors. *Nat Commun* **7**, (2016).
32. Kireev, D. et al. Graphene transistors for interfacing with cells: Towards a deeper understanding of liquid gating and sensitivity. *Sci Rep* **7**, (2017).

Figures

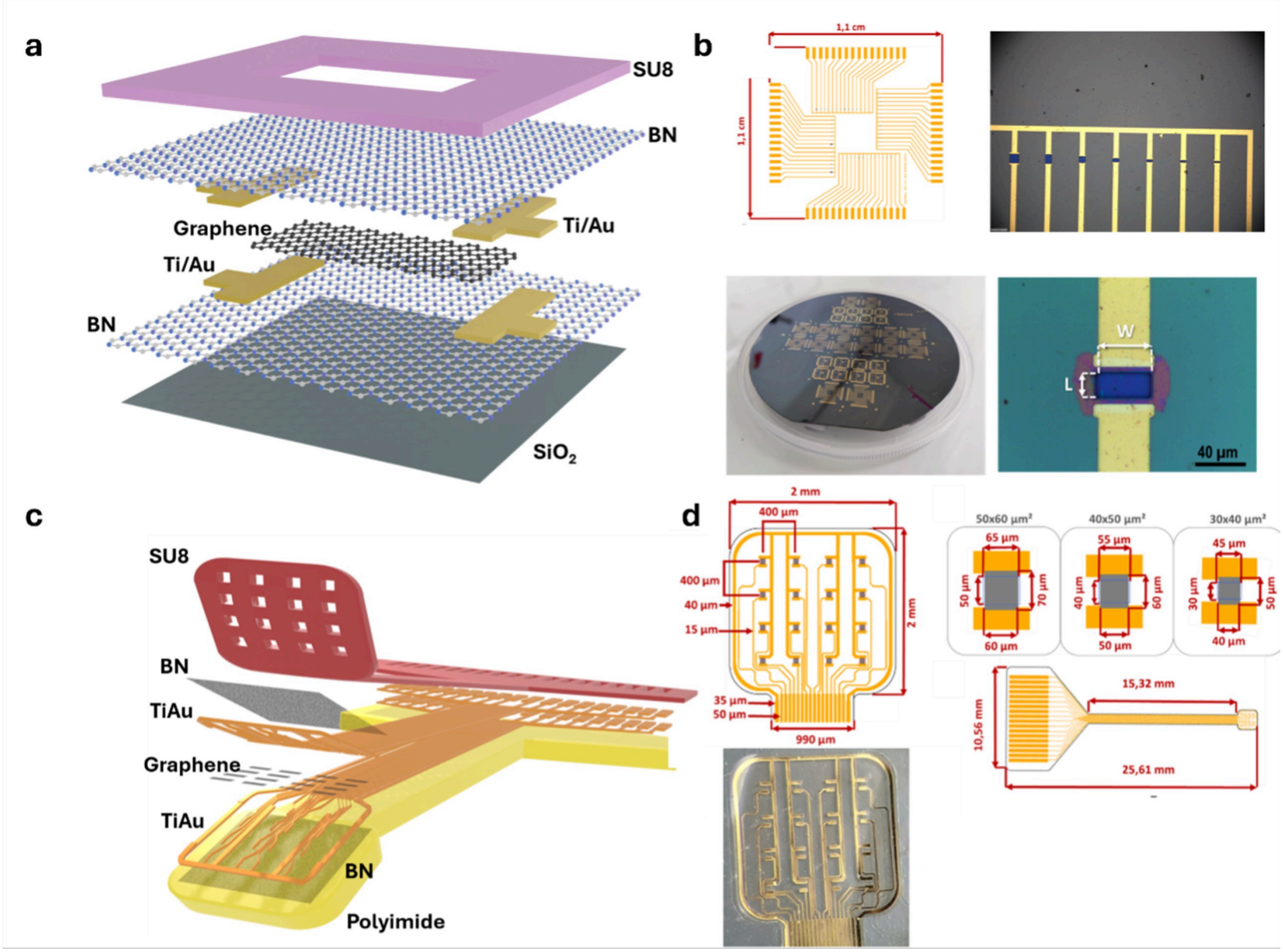


Figure 1

Test devices on SiO_2 and flexible implants on Polymide. a) Material stack of the test devices on SiO_2 b) Schematic and pictures of the test devices consisting of 4 linear arrays of 14 transistors. c) Material stack of the flexible implant on polyimide, d) schematic and pictures of the 4x4 transistor array positioned at the head of the implant.

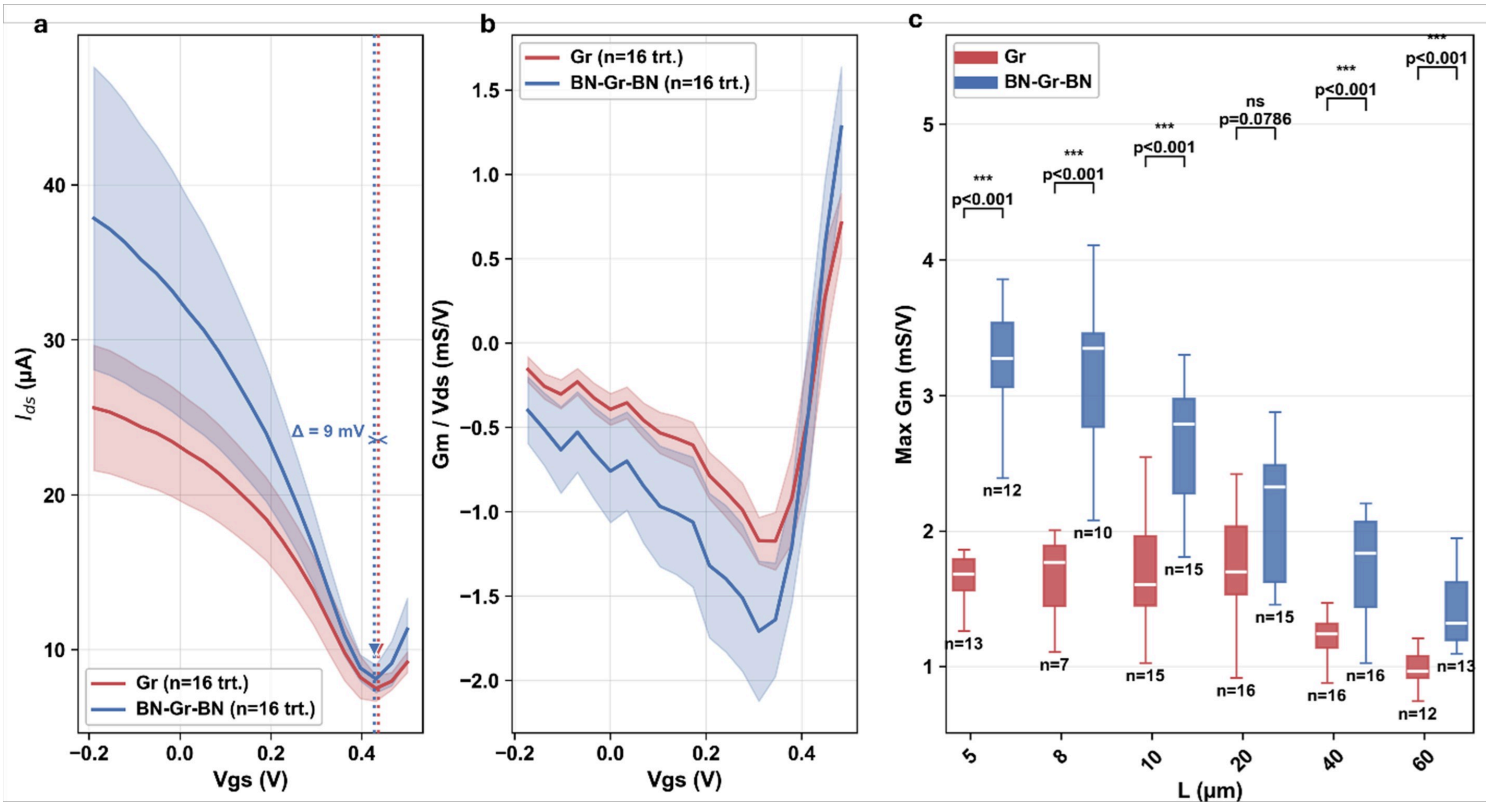


Figure 2

Comparison of the sensitivities of the transistors made of bare (Gr) and encapsulated (BN-Gr-BN) gSGFET : a I_{ds} vs V_{gs} transfer curve for W/L=1, W=40μm (16 BN and 16 bare gSGFET) for V_{ds}=50mV, b) Transconductance vs Vgs for W/L=1, W=40μm (16 BN and 16 Bare gSGFET), c) Max Gm extracted from the Gm vs Vgs curve for L=5,8,10,20,40 and 60μm

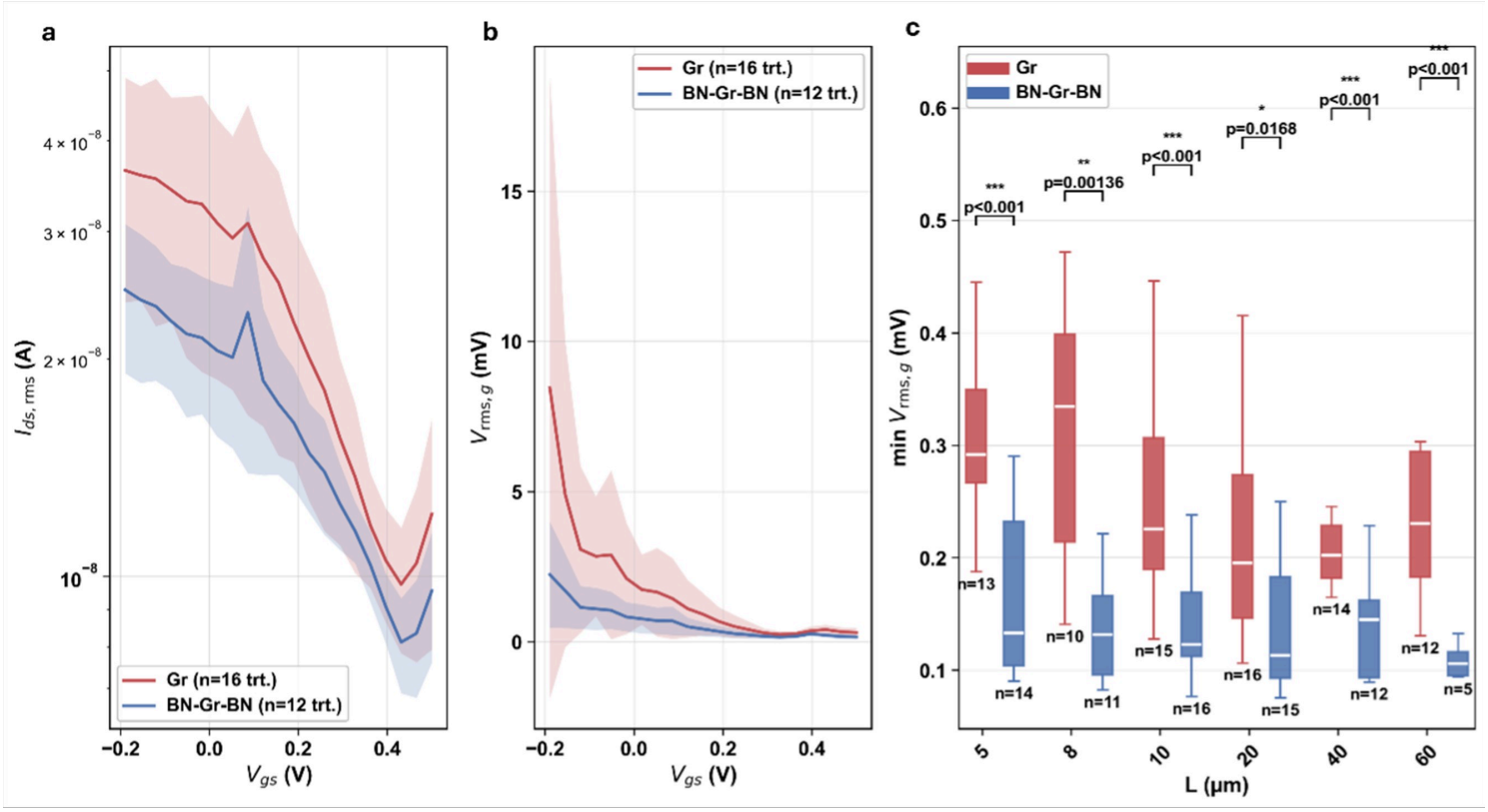


Figure 3

Comparison of the intrinsic noise of the transistors for bare (Gr) and encapsulated (BN-Gr-BN) gSGFET : a) $I_{ds,rms}$ vs V_{gs} transfer curve for W/L=1, W=40μm (12 BN and 16 bare gSGFET), b) V_{rms} vs V_{gs} for W/L=1, W=40μm (12 BN and 16 Bare gSGFET), c) Min V_{rms} extracted from the V_{rms} vs V_{gs} curve for L=5,8,10,20,40 and 60μm

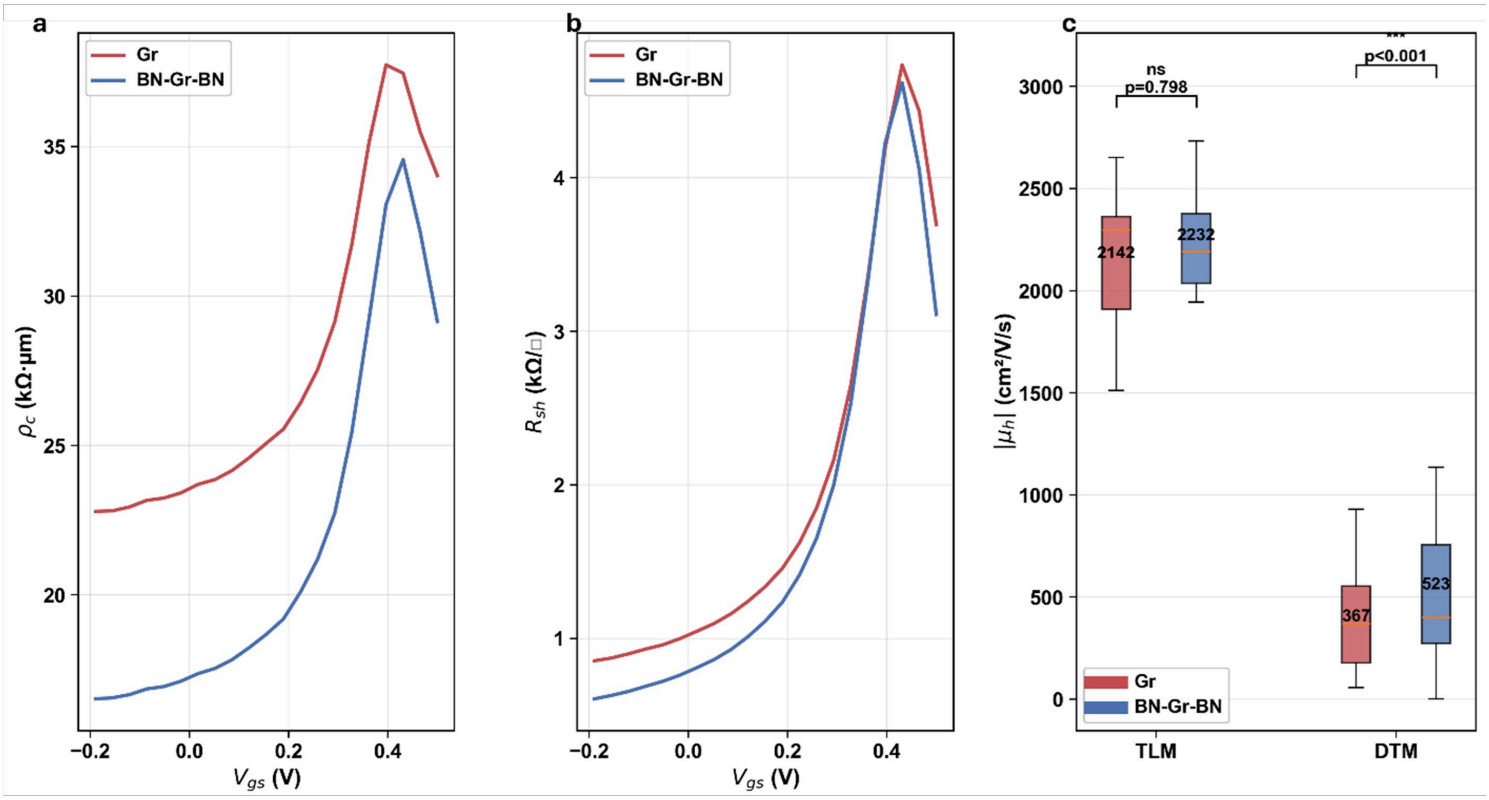


Figure 4

Results from the TLM analysis, a) R contact vs V_{gs}, b) Rsh vs V_{gs} c) Mobility extracted from the TLM and DTM methods

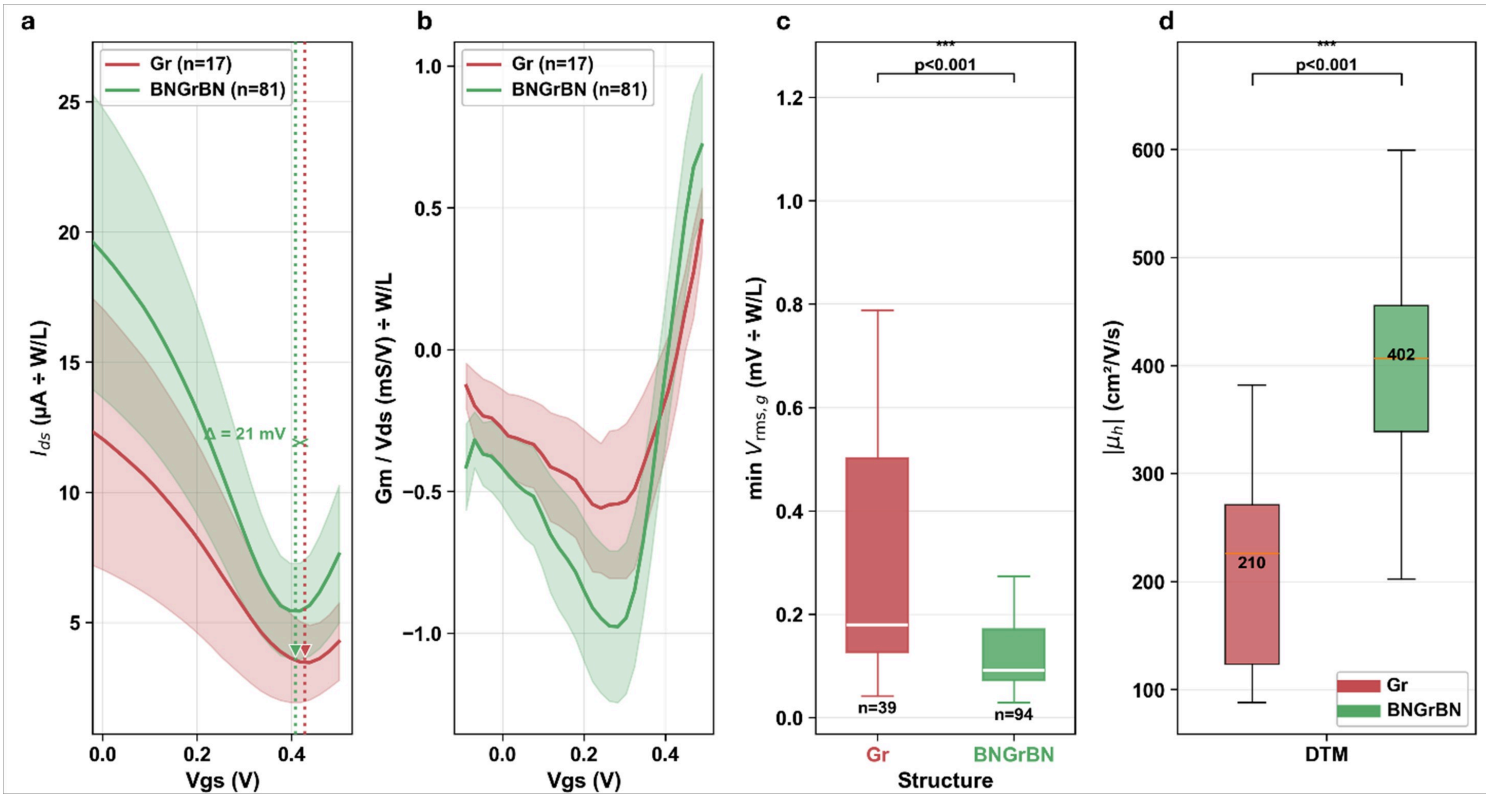


Figure 5

Comparison of the performances of bare and BN-encapsulated gSGFET produced on flexbile Polyimide. a) I_{ds} vs V_{gs} Transfer curve for V_{ds}=50mV, d) Transcondutcance vs V_{gs} curve, c) minVrsm extracted from the V_{rms} vs V_{gs} curve. d) gSGFET channel mobility extracted from the DTM method.

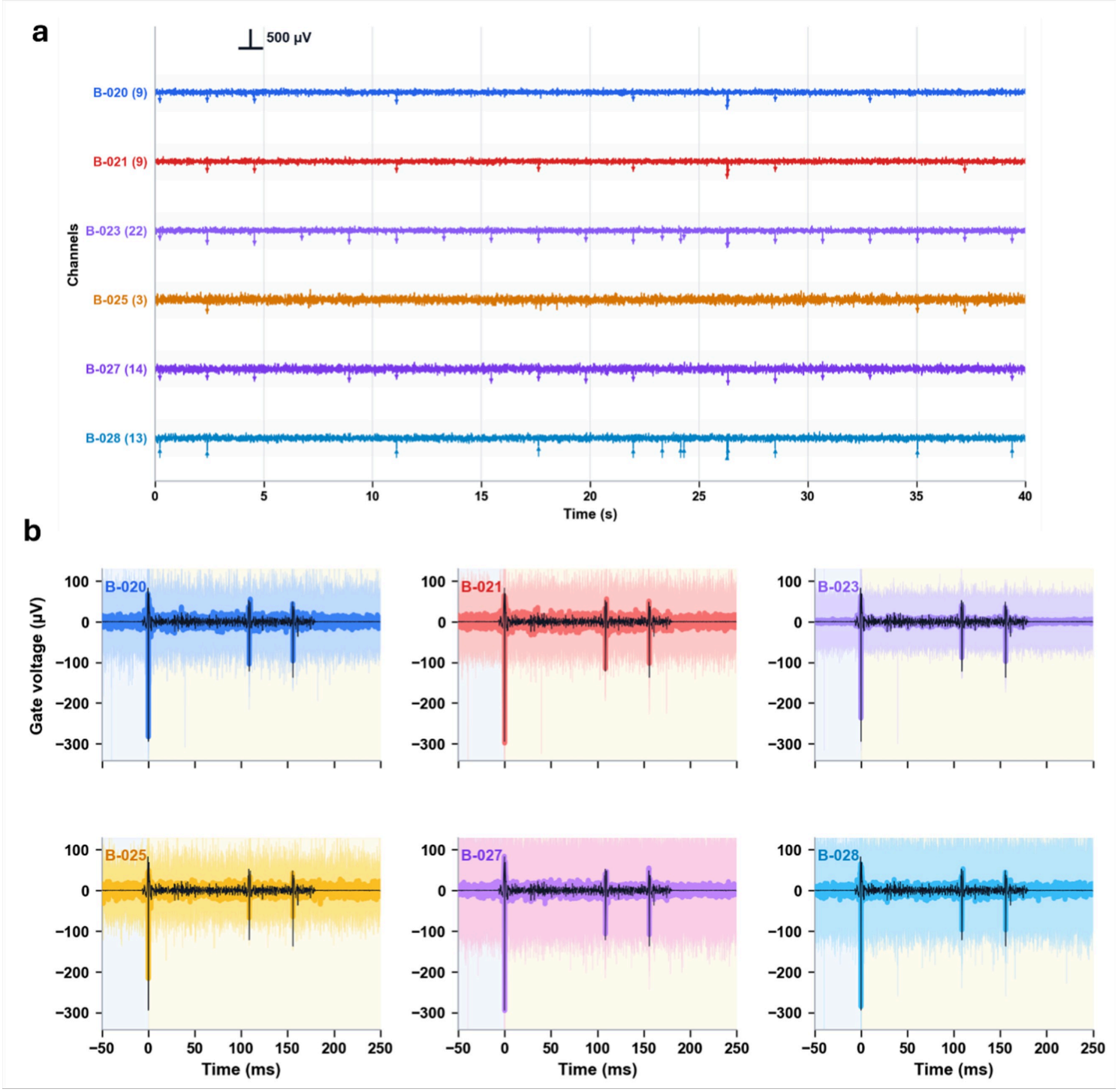


Figure 6

Measurement of an artificial hippocampal spiking activity (High Pass Filtered above 300Hz). a) Signals from the 6 transistors over 40 seconds. b) Overlay of the repeated 300-ms windows of synthetic signal measured on the transistors between -50ms and 250ms with respect to the first spike. The shaded

traces represent the accumulation of all the single events, the bold signal is the mean of all the events, the black signal is the actual synthetic signal applied on the Ag/AgCl gate.

Supplementary Files

This is a list of supplementary files associated with this preprint. Click to download.

- Supplementary2.docx